LETTERS
https://doi.org/10.1038/s41563-019-0457-6

nature materials

Synthetic spin–orbit interaction for Majorana devices

M. M. Desjardins[1,4], L. C. Contamin[1,4], M. R. Delbecq[1], M. C. Dartiailh[1], L. E. Bruhat[1], T. Cubaynes[1], J. J. Viennot[2], F. Mallet[1], S. Rohart[3], A. Thiaville[3], A. Cottet[1] and T. Kontos[1*]

The interplay of superconductivity with non-trivial spin textures is promising for the engineering of non-Abelian Majorana quasiparticles. Spin–orbit coupling is crucial for the topological protection of Majorana modes as it forbids other trivial excitations at low energy but is typically intrinsic to the material[1–7]. Here, we show that coupling to a magnetic texture can induce both a strong spin–orbit coupling of 1.1 meV and a Zeeman effect in a carbon nanotube. Both of these features are revealed through oscillations of superconductivity-induced subgap states under a change in the magnetic texture. Furthermore, we find a robust zero-energy state—the hallmark of devices hosting localized Majorana modes—at zero magnetic field. Our findings are generalizable to any low-dimensional conductor, and future work could include microwave spectroscopy and braiding operations, which are at the heart of modern schemes for topological quantum computation.

Hybrid superconducting nanoscale systems are appealing for fundamental studies of how superconducting correlations are altered when the spin and motion of electrons are coupled[3–7]. When a superconductor is connected to a nanoscale conductor, which hosts few coherent channels, the superconducting correlations give rise to a discrete spectrum inside the superconducting gap, called Andreev bound states. Whereas these states are now well understood in conventional set-ups, their fate in topologically non-trivial materials is the subject of intense activity. One particularly striking feature of those systems is the possible emergence of Majorana modes.

Engineering robust Majorana modes in hybrid quantum devices requires non-collinear spin orientations and superconductivity. This can be achieved through the interplay of a homogeneous magnetic field and spin–orbit coupling. Alternatively, it has been theoretically proposed that these ingredients could be synthesized at the microscopic level by mimicking both a spin–orbit coupling and a Zeeman splitting using a magnetic texture[8–15], as sketched in Fig. 1a. Here, we demonstrate such a device using a single-walled carbon nanotube (our one-dimensional conductor) connected to two superconducting electrodes and coupled to a proximal magnetically textured gate. Within the superconducting gap we observe subgap states (SGSs) whose energies oscillate as a function of the external magnetic field. This is direct evidence that we have induced a large synthetic spin–orbit interaction in the nanotube and observed its interplay with spinful Andreev bound states. We finally observe a zero-bias conductance peak (ZBP) that is stable in the magnetic field, which is compatible with the emergence of Majorana modes in our set-up.

A magnetic field oscillating in space is mathematically equivalent to a Rashba spin–orbit interaction combined with an effective constant magnetic field[8–15]. The period of the oscillations λ sets the spin–orbit energy, and their amplitudes set the magnitude of the effective field. Several methods have been suggested to induce a suitable oscillating field, such as the spin helix arising from nuclear spins interacting through an RKKY interaction[10] or specific patterns of micromagnets[9,11–13]. Such a scheme is expected to be robust to imperfections of the magnetic texture[13,16]. In this work, we elaborate on these theoretical approaches and use a single magnetic material whose domain structure gives rise to a cycloidal-like dipolar field along the nanotube, as depicted in Fig. 1a. Our device is shown in Fig. 1b,e. A single-walled nanotube is stamped onto a magnetic $[Co(1.5\,nm)/Pt(1.0\,nm)]_{10}$/AlOx multilayer bottom gate, which is capacitively coupled to two gate electrodes G and G′ (see Supplementary information). The Co/Pt is expected to have a small pitch and an out-of-plane anisotropy, giving rise to several domains over the length of the nanotube with a strong stray field of about 0.4 T. The magnetic force microscope (MFM) picture shown in Fig. 1e gives evidence of magnetic domains in the bottom gate with a typical size of about 100 nm (see Supplementary Information section 5). An external magnetic field B_{ext} changes the magnetic structure and can therefore reveal the existence of the synthetic spin–orbit interaction.

Superconducting correlations are induced by connecting the nanotube to two Pd(4 nm)/Nb(40 nm) superconducting electrodes. We address the discrete spectrum induced by the superconductor by transport spectroscopy[3–7]. The typical measurement of the differential conductance G_{diff} as a function of source–drain bias V_{sd} is shown in Fig. 1c. The conductance displays a well-defined energy gap of about 550 μeV containing two peaks symmetric with respect to zero bias. These two peaks signal SGSs arising from superconducting correlations. As sketched in Fig. 1d, our measurements are equivalent at low energy to conventional tunnel experiments as a consequence of the finite density of states at the Fermi energy in one of the two superconducting contacts (contact 2). Such a residual density of states in the superconducting leads is systematically observed in our devices (see Supplementary information) and has also been reported by other groups (see for example ref. [17]). The global shape of the conductance curve is well accounted for by the quasi-classical description of superconductivity in the electrodes, based on Usadel equations, and reveals that contact 1 displays a well-defined superconducting hard gap. The large subgap slope is shown to arise mainly from a residual pair breaking in the superconductor (see Supplementary information). The ratio between the high-bias

[1]Laboratoire de Physique de l'Ecole Normale Supérieure, ENS, Université PSL, CNRS, Sorbonne Université, Université Paris Diderot, Sorbonne Paris Cité, Paris, France. [2]Univ. Grenoble Alpes, CNRS, Grenoble INP, Institut Néel, CNRS, Grenoble, France. [3]Laboratoire de Physique des Solides, Université Paris-Saclay, CNRS UMR 8502, Orsay, France. [4]These authors contributed equally: M. M. Desjardins, L. C. Contamin. *e-mail: kontos@lpa.ens.fr

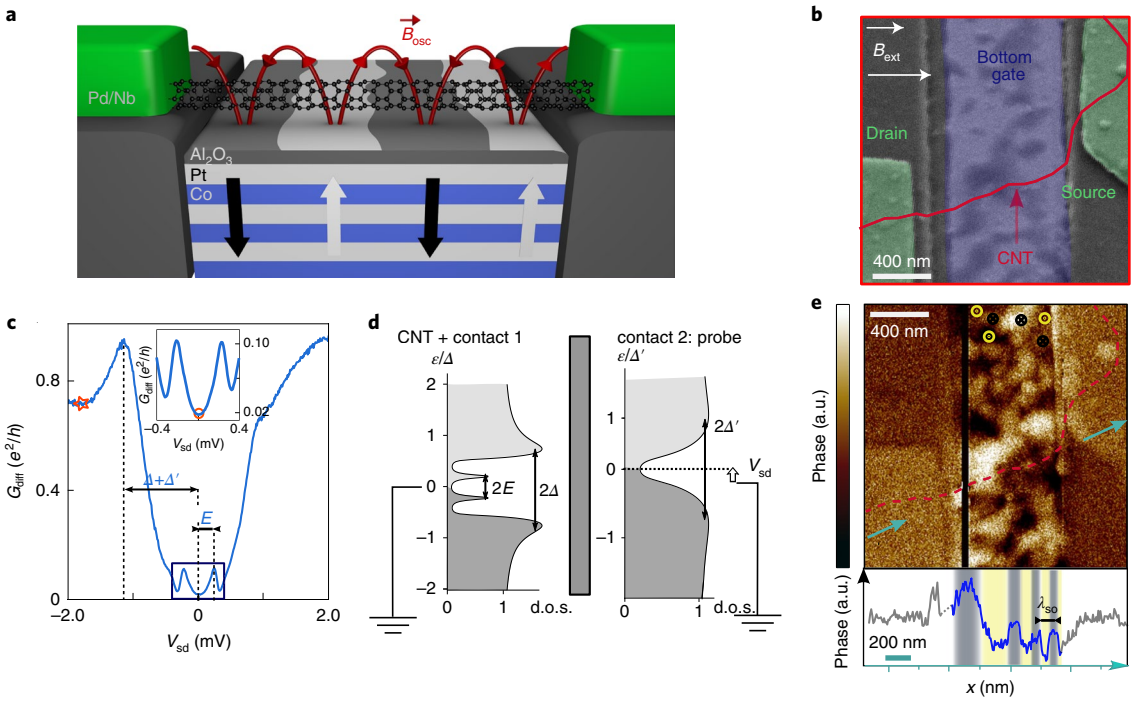

Fig. 1 | Hybrid superconductor–nanotube–magnetic texture set-up. a, Schematic of the multilayer magnetic texture with up and down domains (white and black arrows) inducing the rotating magnetic field B_{osc} in space (red line) leading to the synthetic spin–orbit interaction. **b**, Enlargement of the device showing the single-walled carbon nanotube (CNT, in red). The bottom gate is multilayered Co/Pt. The source and drain superconducting electrodes are made from Pd/Nb. A longitudinal magnetic field B_{ext} can be applied. **c**, Conductance G as a function of source–drain bias V_{sd}; the device displays a well-defined gap (of width $2(\Delta+\Delta')$) with two symmetric SGSs at energy E, enlarged in the inset. The 'hardness' of the gap is measured by the ratio of G values marked by the star and the circle. **d**, Density of states (d.o.s.) as a function of energy ε extracted from the conductance fit. We extract the d.o.s. arising from the coupling between the nanotube and the left superconductor (of gap Δ), and the d.o.s. of the right superconductor (of gap Δ'). The d.o.s. curves are filled with light or dark grey depending on the value of the Fermi function. The right superconductor has a residual d.o.s. at zero bias, allowing for direct spectroscopy of the SGSs. **e**, MFM phase map of the device (in arbitrary units) showing the magnetic texture of the bottom gate. The up and down domains are highlighted by black and yellow circles, respectively. Below the phase map we show the magnetic signal along the direction indicated by the turquoise arrows. The signal is coloured in blue when above the magnetic texture. It displays field modulations (highlighted by the yellow and grey stripes) on a scale of about $\lambda_{so}=200$ nm along the nanotube (dashed red line).

conductance and the zero-bias conductance (which measures the 'hardness' of the gap) is about 45, which compares favourably with the recently reported values in semiconducting nanowires[5].

One of the main findings of our experiments is displayed in Fig. 2b. In this colour-coded map of G_{diff} as a function of V_{sd} and B_{ext}, we observe the evolution of the SGSs under an external magnetic field. Strikingly, they display oscillations with a period of about 600 mT (±10% from one magnetic sweep to another). We can resolve up to three oscillations around the mean energy of 220 μeV, together with the expected slow reduction of the superconducting gap, as shown in Fig. 3a. Such a behaviour is unusual for SGSs and has not been observed in other systems. It stems from the progressive alignment of the magnetic domains with the global magnetic field. This can be understood more precisely from the energy dispersion of electrons subject to a rotating magnetic field $E(\mathbf{K})$ with wavevector $\mathbf{K}$, shown in Fig. 2a. The interference conditions defining the energies of the SGSs are set by the wavevector difference $\Delta\mathbf{K}$ between right-moving and left-moving electrons with non-orthogonal spin eigenstates. A variation of the magnetic domains induces a shift k in the wavevectors $\mathbf{K}$. Near the helical gap, where the spin states are not orthogonal, a term $2kL$ (where L is the confinement length) is added to the interference condition: $E_{SGS}\approx\pm E_{SGS,0}(1+a\cos[2\Delta K(B_{ext})L])$ where $\Delta K(B_{ext})=\Delta K(B_{ext}=0)+2k(B_{ext})$ and a is the relative amplitude of the oscillations. The magnetic field dependence of the SGSs is well accounted for by this formula under the assumption that the spin–orbit strength decays linearly as the field increases, up to a saturation field of about 1 T. Such an evolution of the synthetic spin–orbit energy is supported by magnetic measurements as well as micromagnetic simulations (see Supplementary information). The number of oscillations N sets the range of modulation of $k(B_{ext})$ and therefore allows us to give a lower bound for the induced spin–orbit energy at zero magnetic field: $E_{so}\gtrsim\delta N/2$ (see Supplementary information). From the number of oscillations in Fig. 2b for $B_{ext}>0$ ($N\approx1.5$) and the extracted level spacing ($\delta\approx1.5$ meV, see Supplementary Fig. 2), we deduce $E_{so}\gtrsim1.1$ meV. This is of the order of the simple estimate for a linear spectrum[12,13] $E_{so}=\frac{hv_F}{2\lambda}=\delta\frac{L}{\lambda}$, where v_F is the Fermi velocity in the nanoconductor and $L/\lambda\approx2$ (five domains), inferred from the MFM image in Fig. 1e. This spin–orbit energy is larger than that found in InSb or InAs nanowires (respectively 0.25–1 meV and 0.015–0.135 meV; ref. [18]).

We can reproduce the oscillations of the SGSs with simulations based on the scattering theory, with $\delta\approx1.5$ meV and a superconducting gap $\Delta\approx0.6$ meV extracted from the data, an amplitude of the stray field B_{osc} of 400 mT extracted from the magnetic simulations and a chemical potential close to the helical regime (see Supplementary information). These oscillations are robust to disorder in the magnetic texture and can be qualitatively reproduced from the spatial field evolution inferred from the MFM data of Fig. 1 (see Supplementary information).

To further understand the specificity of our device, we realized a control device without the magnetic texture. We do not observe the presence of subgap states that oscillate with the magnetic field, but

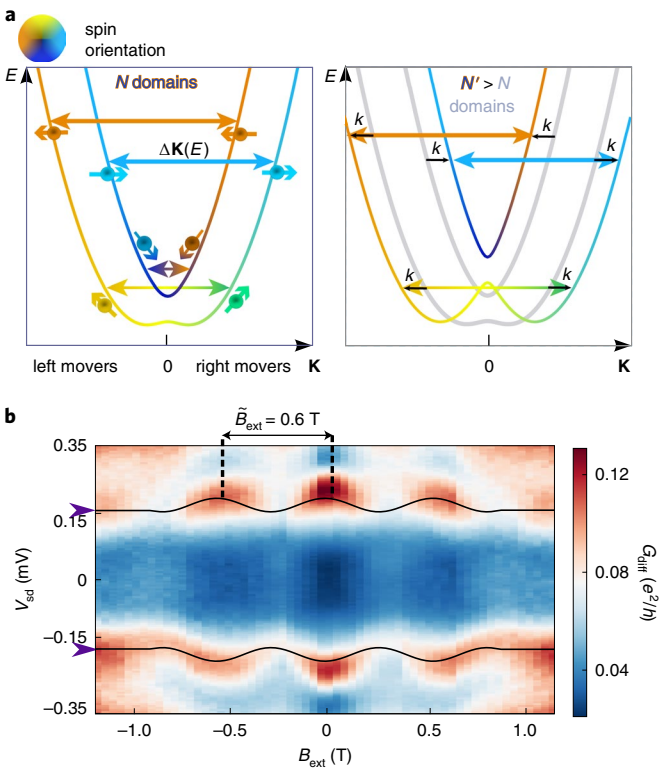

Fig. 2 | Oscillations of the subgap states and synthetic spin–orbit interaction. a, Left, band structure $E(\mathbf{K})$ arising from the synthetic spin–orbit interaction with N domains. The allowed interferences in the finite length system depend on $\Delta\mathbf{K}$, as represented by the coloured arrows. Right, schematics of how the band structure can be tuned by changing the spin–orbit energy (with N' domains, the bands are shifted by k). **b**, Low-bias G map in the V_{sd}–B_{ext} plane showing the oscillations of the SGSs (indicated by purple arrows) as a function of the magnetic field, over a period $\tilde{B}_{ext}$. The black lines are the fit to the theory, as described in the text and in the Supplementary information.

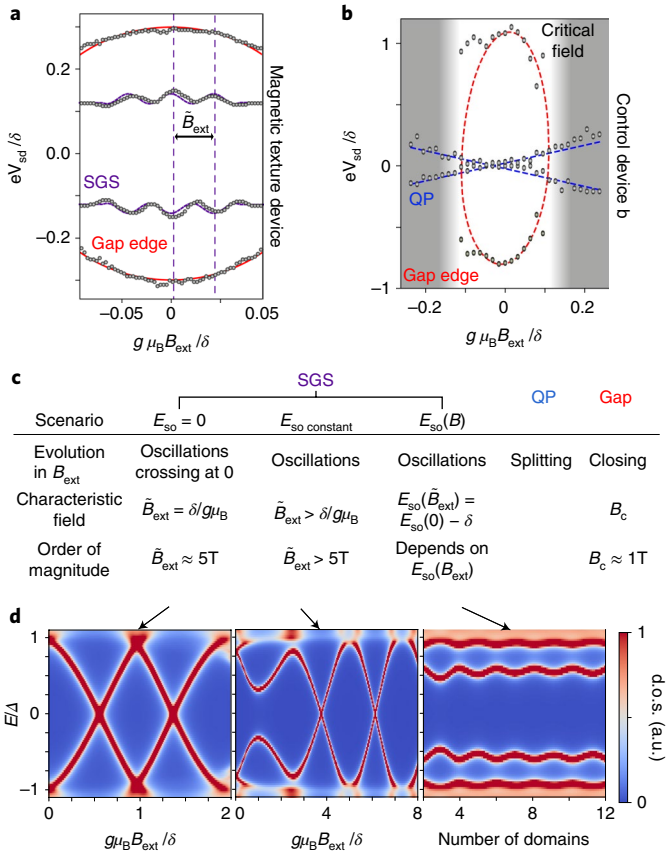

Fig. 3 | Control experiment and phenomenology of subgap states under a magnetic field. a, Transport resonance energies with respect to V_{sd}–B_{ext} in reduced units (defined with respect to δ and to $g\mu_B$). The energy and the gap edge of the SGSs have been extracted from Fig. 2b (grey points), showing either oscillations over a period $\tilde{B}_{ext}$ or a decrease over B_c. Fits to theory are represented in purple and red, respectively (see Supplementary information). **b**, Same plot as in **a** for control device B, without magnetic texture. A quasiparticle resonance (QP, blue) appears within the gap, with a linear blue fit (see Supplementary information). **c**, Table summarizing the phenomenology of the evolution of transport signatures as a function of an external magnetic field, depending on the spin–orbit energy E_{so}. **d**, D.o.s. of a one-dimensional conductor with proximity-induced superconductivity as a function of E/Δ and B_{ext} in the different scenarios of **c**, obtained with tight-binding simulations described in detail in the Supplementary Fig. 14.

only the closing of the superconducting gap and a linear splitting of a quasiparticle resonance coming from a finite density of states in the carbon nanotube (Fig. 3b). The quasiparticle resonance simply splits in B_{ext} with a slope $g\mu_B$ where μ_B is the Bohr magneton (giving a Landé factor $g \approx 3.5$), and the superconducting gap closes over a critical field $B_c \approx 500$ mT. Under a zero or weak constant spin–orbit interaction, SGSs should display crossing oscillations with a period $\tilde{B}_{ext}$ of the order of $\delta/g\mu_B$. This corresponds to $B_{ext} = 5$ T for the SGSs in the control experiment, which explains why they stay pinned to the superconducting gap until it closes. Figure 3c summarizes possible behaviours for the SGSs under a magnetic field. They are illustrated in Fig. 3d with tight-binding simulations of the density of state in a one-dimensional conductor connected to a superconductor. The left and central panels describe the evolution of SGSs in a conductor with no (left) and intrinsic (centre) spin–orbit interaction as a function of an external magnetic field. The right panel describes the evolution of SGSs subject to a cycloidal magnetic field under a variation of its period. In the magnetic device, the period of the oscillations with the external field is only compatible with a modulation of the induced spin–orbit interaction through the progressive alignment of the magnetic domains. The oscillations thus point unambiguously to the non-trivial character of the observed SGSs.

The large measured value of the spin–orbit interaction is an important prerequisite for driving a hybrid device into the topological regime, where zero-energy Majorana modes can emerge. In all the devices experimentally investigated so far, this has only been pursued by applying a large external magnetic field with severe constraints on network designs, Majorana mode lifetimes and coupling to superconducting quantum circuits. By contrast, our magnetic texture is equivalent to both a finite, large spin–orbit interaction and an external magnetic field. Our device could host Majorana modes without any external magnetic field, thus lifting these constraints.

In our set-up, superconductivity is induced from the side into the helical region through the superconducting proximity effect. Although this is a slight difference compared with other experiments, it can in principle lead to Majorana modes[18–21] (see also Supplementary information for a more developed discussion of this possibility). In Fig. 4a, at zero external field, a ZBP emerges when gate G is tuned at $V_g > 0.5$–0.6 V. We note that this gate does not affect the SGSs or the superconducting gap; it affects only the appearance of the ZBP along with a slight increase in the conductance background. The ZBP has a width of about 150 μeV, as shown in Fig. 4b, and a height of about $0.05\,e^2/h$, comparable to the recent

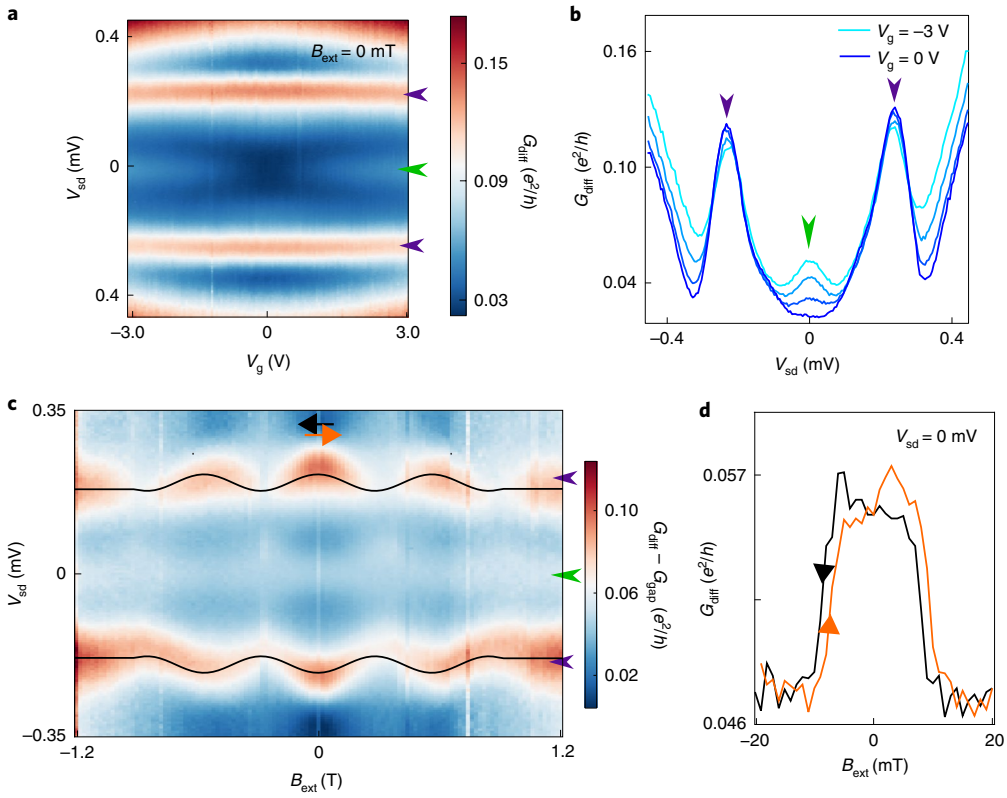

Fig. 4 | Zero-bias peak. a, Map of G in the V_{sd}–V_g plane showing the appearance of a ZBP when gate G is tuned. The ZBP position is indicated by a green arrow and the SGSs by purple arrows. **b**, G profiles for $V_g = 0, -1, -2, -3$ V. **c**, Map of G at $V_g = -3$ V in the V_{sd}–B_{ext} plane showing the evolution of the zero-energy peak as a function of the in-plane magnetic field. The overall background G_{gap} arising from the superconducting gap has been subtracted for clarity (see Supplementary Fig. 3). The black lines correspond to the same fit as Fig. 2b. The orange and black arrows indicate the magnetic field range of panel **d**. **d**, Low magnetic field conductance G_{diff} profile map in the V_{sd}–B_{ext} plane for $V_g = -3$ V displaying the large magnetoresistance of the zero-bias peak. The orange and black arrows represent the direction of the magnetic field sweep.

findings in semiconducting nanowires (see for example ref. [7]; this reduced height can have several origins[22]). In our case, the energy dependence of the probe contact density of states lowers the ZBP conductance, which cannot be mapped directly onto its spectral weight. In Fig. 4d, we measure a large magnetoresistance of 20% for this ZBP, accompanied by a hysteretic behaviour, which is a signature of the effect of the magnetic texture. This strong dependence at small magnetic fields could come from local reconfiguration of the magnetic domains. This is consistent with the expected spatial localization of the state corresponding to the ZBP. In contrast, the finite energy SGSs are not affected by a small magnetic field (see Supplementary Figs. 7 and 16). Finally, Fig. 4c displays a conductance map in which the ZBP is robustly pinned at zero energy at a large external magnetic field. These features are compatible with the ZBP, indicating the presence of Majorana zero modes (see Supplementary information for more control experiments).

To conclude, we have demonstrated a device with a synthetic spin–orbit interaction induced by a proximal ferromagnetic multilayer producing an inhomogeneous local magnetic field. This spin–orbit interaction extensively modifies the superconducting correlations induced by superconducting contacts and allows us to observe a ZBP suggestive of a Majorana mode without any external magnetic field. By relaxing the constraint of an external magnetic field, our set-up is suitable for advanced experiments that would unambiguously[23–25] characterize Majorana modes with the tools of circuit quantum electrodynamics (cQED) circuits[26–29]. The built-in two-dimensional pattern of our magnetic textures may also be of interest for braiding schemes[30], which will require networks of Majorana modes with local and autonomous generation of topological superconductivity.

Online content

Any methods, additional references, Nature Research reporting summaries, source data, statements of code and data availability and associated accession codes are available at https://doi.org/10.1038/s41563-019-0457-6.

Received: 4 April 2019; Accepted: 15 July 2019;
Published online: 19 August 2019

References

1. Oreg, Y., Refael, G. & Von Oppen, F. Helical liquids and Majorana bound states in quantum wires. *Phys. Rev. Lett.* **105**, 177002 (2010).
2. Lutchyn, R. M., Sau, J. D. & Das Sarma, S. Majorana fermions and a topological phase transition in semiconductor-superconductor heterostructures. *Phys. Rev. Lett.* **105**, 077001 (2010).
3. Zhang, H. et al. Quantized Majorana conductance. *Nature* **556**, 74–79 (2018).
4. Das, A. et al. Zero-bias peaks and splitting in an Al-InAs nanowire topological superconductor as a signature of Majorana fermions. *Nat. Phys.* **8**, 887–895 (2012).
5. Albrecht, S. M. et al. Exponential protection of zero modes in Majorana islands. *Nature* **531**, 206–209 (2016).
6. Nadj-Perge, S. et al. Observation of Majorana fermions in ferromagnetic atomic chains on a superconductor. *Science* **346**, 602–607 (2014).
7. Deng, M. T. et al. Majorana bound state in a coupled quantum-dot hybrid-nanowire system. *Science* **354**, 1557–1562 (2016).
8. Braunecker, B., Japaridze, G. I., Klinovaja, J. & Loss, D. Spin-selective peierls transition in interacting one-dimensional conductors with spin-orbit interaction. *Phys. Rev. B* **82**, 045127 (2010).

9. Klinovaja, J., Stano, P. & Loss, D. Transition from fractional to Majorana fermions in Rashba nanowires. *Phys. Rev. Lett.* **109**, 236801 (2012).
10. Klinovaja, J., Stano, P., Yazdani, A. & Loss, D. Topological superconductivity and Majorana fermions in RKKY systems. *Phys. Rev. Lett.* **111**, 186805 (2013).
11. Kjaergaard, M., Wölms, K. & Flensberg, K. Majorana fermions in superconducting nanowires without spin-orbit coupling. *Phys. Rev. B* **85**, 020503(R) (2012).
12. Egger, R. & Flensberg, K. Emerging dirac and Majorana fermions for carbon nanotubes with proximity-induced pairing and spiral magnetic field. *Phys. Rev. B* **85**, 235462 (2012).
13. Klinovaja, J. & Loss, D. Giant spin-orbit interaction due to rotating magnetic fields in graphene nanoribbons. *Phys. Rev. X* **3**, 011008 (2013).
14. Nadj-Perge, S., Drozdov, I. K., Bernevig, B. A. & Yazdani, A. Proposal for realizing Majorana fermions in chains of magnetic atoms on a superconductor. *Phys. Rev. B* **88**, 020407 (2013).
15. Pientka, F., Glazman, L. I. & Von Oppen, F. Topological superconducting phase in helical Shiba chains. *Phys. Rev. B* **88**, 155420 (2013).
16. Choy, T.-P., Edge, J. M., Akhmerov, A. R. & Beenakker, C. W. J. Majorana fermions emerging from magnetic nanoparticles on a superconductor without spin-orbit coupling. *Phys. Rev. B* **84**, 195442 (2011).
17. Su, Z. et al. Mirage Andreev spectra generated by mesoscopic leads in nanowire quantum dots. *Phys. Rev. Lett.* **121**, 127705 (2018).
18. Yokoyama, T., Eto, M. & Nazarov, Y. V. Josephson current through semiconductor nanowire with spin-orbit interaction in magnetic field. *J. Phys. Soc. Jpn.* **82**, 054703 (2013).
19. San-Jose, P., Cayao, J., Prada, E. & Aguado, R. Majorana bound states from exceptional points in non-topological superconductors. *Sci. Rep* **6**, 21427 (2016).
20. Keidel, F., Burset, P. & Trauzettel, B. Tunable hybridization of Majorana bound states at the quantum spin Hall edge. *Phys. Rev. B* **97**, 075408 (2018).
21. Peñaranda, F., Aguado, R., San-Jose, P. & Prada, E. Quantifying wave-function overlaps in inhomogeneous Majorana nanowires. *Phys. Rev. B* **98**, 235406 (2018).
22. Danon, J., Hansen, E. B. & Flensberg, K. Conductance spectroscopy on Majorana wires and the inverse proximity effect. *Phys. Rev. B* **96**, 125420 (2017).
23. Liu, J., Potter, A., Law, K. & Lee, P. Zero-bias peaks in the tunneling conductance of spin-orbit-coupled superconducting wires with and without Majorana end-states. *Phys. Rev. Lett.* **109**, 267002 (2012).
24. Rainis, D., Trifunovic, L., Klinovaja, J. & Loss, D. Towards a realistic transport modeling in a superconducting nanowire with Majorana fermions. *Phys. Rev. B* **87**, 024515 (2013).
25. Liu, C.-X., Sau, J. D., Stanescu, T. D. & Das Sarma, S. Andreev bound states versus Majorana bound states in quantum dot-nanowire-superconductor hybrid structures: trivial versus topological zero-bias conductance peaks. *Phys. Rev. B* **96**, 075161 (2017).
26. Cottet, A., Kontos, T. & Douçot, B. Squeezing light with Majorana fermions. *Phys. Rev. B* **88**, 195415 (2013).
27. Van Woerkom, D. J. et al. Microwave spectroscopy of spinful Andreev bound states in ballistic semiconductor Josephson junctions. *Nature Phys.* **13**, 876–881 (2017).
28. Väyrynen, J. I., Rastelli, G., Belzig, W. & Glazman, L. I. Microwave signatures of Majorana states in a topological Josephson junction. *Phys. Rev. B* **92**, 134508 (2015).
29. Dartiailh, M. C., Kontos, T., Douçot, B. & Cottet, A. Direct cavity detection of Majorana pairs. *Phys. Rev. Lett.* **118**, 126803 (2017).
30. Fatin, G. L., Matos-Abiague, A., Scharf, B. & Žutić, I. Wireless Majorana bound states: from magnetic tunability to braiding. *Phys. Rev. Lett.* **117**, 077002 (2016).

Acknowledgements

We are indebted to B. Leridon for the SQUID measurements and to K. Bouzehouane for MFM measurements. We acknowledge J. Palomo, M. Rosticher, A. Pierret and A. Denis for technical support. L.C.C. acknowledges the support from a Foundation CFM-J.P. Aguilar grant. The devices were made within the consortium Salle Blanche Paris Centre. This work is supported by ERC Starting Grant CIRQYS and grants from Région Ile de France and the ANR FunTheme.

Author contributions

M.M.D. set up the experiment, and L.C.C. made the devices and carried out the measurements with the help of T.K. L.C.C. and M.M.D. performed the analysis of the data with inputs from T.K. L.C.C. and M.R.D. carried out the fabrication, measurement and analysis of the control experiment. M.M.D., J.J.V. and L.E.B. contributed through early experiments and the development of the nanofabrication process. T.C. and F.M. contributed to the experimental aspects. M.C.D. developed the data acquisition software. S.R. and A.T. developed the magnetic texture process and carried out the magnetic characterization with M.M.D. and L.C.C. M.M.D., L.C.C., M.R.D., T.K. and A.C. carried out the theory for the ABS oscillations. M.M.D. studied the tight-binding model using a framework developed by M.C.D. with theoretical insight from A.C. T.K., M.M.D., L.C.C., M.R.D. and A.C. co-wrote the manuscript with inputs from all the authors.

Competing interests

The authors declare no competing interests.

Additional information

Supplementary information is available for this paper at https://doi.org/10.1038/s41563-019-0457-6.

Reprints and permissions information is available at www.nature.com/reprints.

Correspondence and requests for materials should be addressed to T.K.

Methods

Fabrication of the devices and measurement techniques. A 150-nm-thick Nb film is evaporated on a high-resistivity Si substrate at a rate of 1 nm/s and a pressure of 10^{-9} mbar. A microwave cavity (see Supplementary Information) is subsequently made using photolithography combined with reactive ion etching (SF_6 process). An array of bottom gates is then made with two e-beam lithography steps in a 100 μm^2 opening of the cavity ground plane near the central conductor. First, we etch 750 nm × 36 μm trenches of 60 nm depth with reactive ion etching (CHF_3 process). Second, we deposit a Ta(4 nm)/Pt(4.5 nm)/[Co(1.5 nm)/Pt(0.9 nm)]$_{10}$/Pt(3.6 nm)/Al(4 nm) multilayer bottom gate inside the trenches, 100 nm thinnger. This magnetic stack is chosen to promote spontaneously magnetic textures consisting of magnetic stripes with up and down magnetization directions with a narrow period. The Pt/Co interfaces induce a perpendicular anisotropy energy that partially compensates for the shape anisotropy that would induce an in-plane magnetization. The thickness of the Co and the number of repetitions are chosen to increase the dipolar energy (the driving force of the stripes formation) and to maximize the stray field above the sample to about ±400 mT. All the layers in the sample are strongly coupled through their magnetic stray field and belong to a single and continuous magnetic texture. Carbon nanotubes are grown with the chemical vapor deposition technique at about 900 °C using a methane process on a separate quartz substrate and stamped above the bottom gates[20]. The quartz substrate was previously processed so that a few pillars with a height of 4 μm and surface areas of 10 μm × 5 μm are aligned with the cavity openings and come in contact when stamping (see the stamping marks in Fig. 1a). The nanotubes are then localized, and those that correctly lie on a bottom gate are contacted with Pd(4 nm)/Nb(40 nm). The Nb layer is evaporated at a rate of 1 nm s^{-1} and pressure of 10^{-9} mbar while the substrate is cooled to 0 °C. During this last e-beam lithography and evaporation step, gate electrodes are also patterned to capacitively couple the bottom gate to a d.c. gate voltage $V_{g'}$ (corresponding to gate G′) and to the a.c. potential of the central conductor of the cavity. An additional gate G is capacitively coupled to the central core of the cavity, and a voltage V_g can be applied.

The d.c. measurements are made using standard lock-in detection techniques with a modulation frequency of 137 Hz and an amplitude of 10 μV. The base temperature of the experiment is 18 mK. An external magnetic field can be applied along the direction of the tube.

Three control devices were also fabricated to investigate SGSs (their transport characteristics are presented in Supplementary Figs. 8 and 9). Device A was fabricated with the same technique as the magnetic device, with an Ni/AlOx bottom gate and Pd/Al superconducting contacts. Devices B and C were fabricated with a slightly different fabrication technique; the Co/Pt gate was replaced by a Ti(5 nm)/Al(100 nm) bottom gate, and the superconducting contacts are in Nb/Pd.

Conductance peaks for device B are reproduced in Fig. 3b. The chemical potential is tuned through an additional (NbOx) gate that forms a fork around the bottom gate, noted V_g in the characterization. In a similar fashion, the carbon nanotube was connected to two Nb(150 nm)/Pd(4 nm) superconducting electrodes. The d.c. measurements are made at a modulation frequency of 77.77 Hz and an amplitude of 15 μV since the signal is smaller.

To summarize the reproducibility of our devices, we have fabricated more than ten magnetic texture devices, but only one had the right parameters to probe the physics of subgap states (obtaining large tunnel rates to the superconducting leads, in particular). We have also fabricated about 20 control devices without the Co/Pt texture, among which only 3 had sufficiently good contacts to measure transport. All the devices that had good enough superconducting contacts to perform transport measurements (one device with Co/Pt texture and three without) were of S-CNT-S′ type with S having a hard gap and S′ having a residual in-gap density of states.

Data availability

The authors declare that the main data supporting the findings of this study are available within the article (main text, methods and Supplementary information). Extra data are available from the corresponding author on reasonable request.

Code availability

The codes used in this paper are available at https://github.com/Exopy.